ChemComm

RSC Publishing

COMMUNICATION

View Article Online
View Journal | View Issue

Cite this: *Chem. Commun.*, 2013, **49**, 892

Received 23rd October 2012,
Accepted 4th December 2012

DOI: 10.1039/c2cc37702k

www.rsc.org/chemcomm

A novel multifunctional nano-platform with enhanced anti-cancer and photoacoustic imaging modalities using gold-nanorod-filled silica nanobeads†

Po-Jung Chen,[a] Shang-Hsiu Hu,[a] Chih-Tai Fan,[b] Meng-Lin Li,[b] You-Yin Chen,[c] San-Yuan Chen*[a] and Dean-Mo Liu*[a]

The novel nano-seaurchin structure is characteristic of high-density and well-dispersed gold nanorods in one mesoporous silica nanobead. This nanoplatform provided increased photothermal stability, stable photoacoustic signal and highly efficient hyperthermia effect both *in vitro* and *in vivo*, indicating a powerful theranostic modality.

A new imaging system, photoacoustic imaging, is a nonionizing and noninvasive imaging modality that combines the advantages of both optical and acoustic functionalities.[1] In photoacoustic imaging, intensity modulated electromagnetic radiation, *e.g.*, a beam of pulsed laser light, is directed at the imaging target. The light absorbed and converted to an outgoing thermoacoustic wave can be detected by an ultrasound transducer and used to reconstruct images.[2] In recent studies, photoacoustic imaging has been demonstrated successfully using gold nanorods, nanocages and nanoshells with high and tunable optical absorption cross section.[3] However, upon photoacoustic imaging, gold nanoobjects are exposed to high energy nanosecond laser pulses and easily collapse to their original shape because of the generated heat, resulting in a reduction in absorption cross section and considerable variation of optical behaviors and reduction of imaging capability.[4] One important strategy to stabilize the nanostructure of gold nanoobjects is to physically trap the nanoobject in a confined and thermally-stable entity, such as carbon, silica and polyethylene glycol (PEG).[5] However, most chemical modifications are complex, time-consuming and even lead to risk of losing the original function of the starting nanomatrix.[6] Therefore, a major challenge is how to engineer molecular probes with integrated functionalities while still maintaining compact geometry, photothermal stability and biocompatibility.

Recently, gold nanostructures (AuNSs), in a geometric form of spherical nanoparticles, nanorods and/or nanoshells, have been actively investigated and well recognized as a promising and versatile platform for cancer treatments.[7] A key factor contributing to clinical therapies requires adequate accumulation of nanometric gold in the tumor site and sufficient tumor penetration of the excitation energy.[8] However, in current studies, the tumor delivery of AuNSs has relied on an enhanced permeability and retention (EPR) effect, a result of tumor blood vessel leakiness due to a state of ongoing angiogenesis,[9] which thus has not been very efficient because AuNSs are easily aggregated (accumulated) in a localized tumor site, which makes it difficult to eradicate the whole tumor tissue with this approach. Therefore, the development of multifunctional nanoobjects enabling new imaging and therapy modalities beyond the above-mentioned intrinsic limitations of individual components is essential.

Here, we report a new nano-seaurchin structure where the nanoporosity within uniform mesoporous silica nanobeads was filled with gold nanorods, giving a multifunctional nanoprobe capable of performing photoacoustic imaging and thermotherapeutics. This multifunctional nanoprobe was fabricated in a facile, stepwise procedure, including (1) formation of 3-aminopropyltrimethoxysilane-functionalized mesoporous silica nanoparticles with pore size >10 nm, (2) seeding of gold nanoparticles in the cavity of porous silica, (3) confined growth of gold initiated from the embedded gold precursor, forming high density gold nanorods conforming with the nanoporosity of the porous silica. This multifunctional nanoprobe, to our knowledge, provides exceptionally high photothermal stability and tunable heating capability, which offers potential advantages for anti-cancer purposes and photoacoustic imaging.

Fig. 1a illustrates the synthesis of mesoporous silica nanobeads with gold nanorod filled nano-seaurchin structure (AuRNBs). The first step is to synthesize the 3-aminopropyltrimethoxysilane-functionalized mesoporous silica nanobeads using an organic template method. The morphology and particle size of the porous nanobeads were analyzed using scanning electron microscopy and transmission electron microscopy, as shown in Fig. 1b and c, respectively. Nearly monodispersed spherical porous nanobeads

[a] *Department of Materials Sciences and Engineering, National Chiao Tung University, Hsinchu, 300, Taiwan. E-mail: sanyuanchen@mail.nctu.edu.tw, deanmo_liu@yahoo.ca*
[b] *Department of Electrical Engineering, National Tsing Hua University, Hsinchu, 300, Taiwan*
[c] *Institution of Biomedical Engineering, National Yang-Ming University, Taipei, Taiwan*

† Electronic supplementary information (ESI) available. See DOI: 10.1039/c2cc37702k

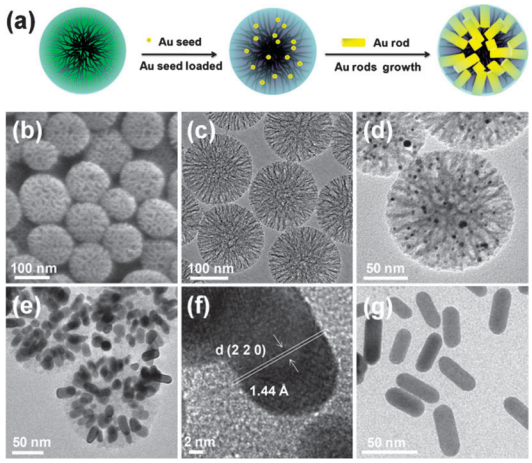

Fig. 1 (a) Schematic illustration of the synthesis and structure of the mesoporous silica nanobeads with gold nanorod filled structure (AuRNBs). (b) SEM image and (c) TEM image of porous nanobeads. (d) TEM image of the gold seeds formed inside silica nanobeads (AuSNBs). (e) TEM image of mesoporous silica nanobeads with gold nanorod pore-filled structure (AuRNBs). (f) High resolution TEM image of mesoporous silica nanobead gold nanorod pore-filled structure, which showed a lattice spacing of 1.44 Å for Au nanorod (2 2 0) plane. (g) TEM image of well-defined AuRNBs after removing the silica matrix by NaOH etching.

with an average diameter of 125 nm were observed. As is well-known, gold species, including $AuCl_4^-$ and metallic gold, have a high affinity for amino groups due to electrostatic and/or coordinate interactions. The selective modification of the inner surface of the silica nanobeads with amino groups allows the retention of gold species inside the templates during the chemical adsorption of gold seeds. Thus, the gold seeds were intermolecularly inserted to form a stable, interdigitated configuration. After seeding, gold nanoparticles of about 4 nm in size were formed within the porosities of each silica nanobead (Fig. 1d). No obvious nucleation of the gold seeds deposited along the outermost regions of the silica nanobeads has been observed. Furthermore, the key in the growth step of gold seeds is to maintain a low reaction rate and minimize self-nucleation events. For example, we used ascorbic acid as a weaker reducing agent to replace $NaBH_4$ for the reduction of gold salt. After the seed-carrying nanobeads (AuSNBs) were immersed into the gold growth solution, the growth of gold seeds occurred as evidenced by the color change of the mixture, forming silica nanobeads with AuR-filled structures, wherein the Au grew into a nanorod geometry to fill up the nanocavities of the silica matrix (Fig. 1e and f). The silica nanobeads with gold-nanorod-filled structures (AuRNBs) were further evidenced using energy-dispersive X-ray spectroscopy by TEM (Fig. S1†). Furthermore, well-defined gold nanorods were obtained after dissolving the silica matrix by NaOH etching, as shown in Fig. 1g, where the resulting gold nanorods exhibited a uniform size, substantiating a successful Au growth in confined nanospace.

The growth of gold nanorods with different aspect ratios can be easily manipulated by adjusting the silver ion ($AgNO_3$) content in the growth solution. Fig. 2a shows the effect of adding identical growth solution to 20–100 μL of 0.01 M $AgNO_3$ solution. It can be seen that by controlling the silver concentration, the longitudinal plasmonic band of AuRNBs can be adjusted. Structural morphology and size distribution of the Au nanorods of varying aspect ratios were examined using TEM as shown in Fig. 2b, Fig. S3 and Table S1†, respectively. With the average aspect ratio increasing from 2.3 to 4.5, the longitudinal plasmonic band underwent an extensive red-shift from 636 to 821 nm, which is close to the values predicted by theoretical calculations ($\lambda_{max} = 95R + 420$ nm; R = aspect ratio).[10]

The thermal stability of pure gold nanorods, as well as AuRNBs was compared using UV-Vis spectroscopy. The longitudinal plasmonic peak is a good indicator for shape changes of the nanorods, because the peak position strongly depends on the aspect ratio of the nanorods. Indeed, after irradiating the pure AuR and AuRNBs with 10 mJ cm^{-2} pulse laser with 100–1500 laser pulses, the shape and intensity of the longitudinal plasmonic peak were changed in all cases (Fig. 2c and d). Fluences above 10 mJ cm^{-2} induced a 30% reduction in amplitude for the gold nanorods after 100 laser pulses, while about 10% reduction was observed for AuRNBs. Further increasing the number of laser pulses led to a dramatic decrease in the spectral amplitude, a strong blue shift of the longitudinal peak, and a strong increase of the absorption in the 600–700 nm range, which are all consistent with a rounding of the gold nanorods. In contrast, the porous silica matrix introduced a stabilizing effect on the gold nanorods. Above 1000 laser pulses, the peak only slightly decreased, and no shoulder in the 600–700 nm range was evolved. It is therefore clear that the gold nanorods physically confined within the porous silica nanobeads were stabilized from structural collapse, ensuring high and stable emitting efficiency, suggesting that the newly-synthesized AuRNBs can be a promising contrast substance for photoacoustic imaging application.

The photoacoustic signal produced by AuRNBs is observed to be linearly dependent on the concentration as shown in Fig. S4†. For *in vivo* measuring the efficiency of the photoacoustic signal, mice with CT26 tumor (mouse colon cancer) were intravenously injected from tail vein with AuR (200 μL, 1 mg mL^{-1}) and AuRNBs solution (200 μL, 1 mg mL^{-1}).

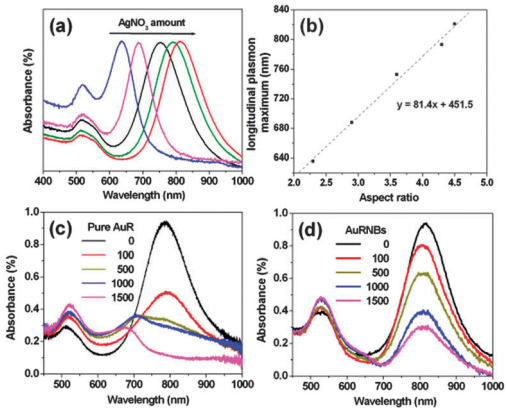

Fig. 2 (a) Extinction spectra of AuRNBs by controlling the aspect ratio during varying the silver ion ($AgNO_3$) content in the growth solution. (b) The longitudinal plasmon maximum effect with different aspect ratio. Measured UV-Vis extinction spectra of (c) pure AuR and (d) AuRNBs before and after irradiation with various laser pulses.

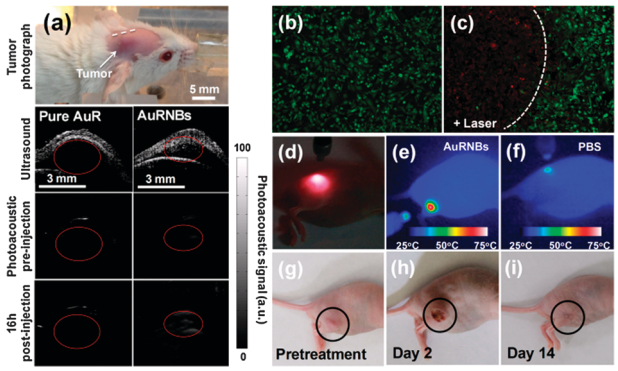

Fig. 3 (a) Ultrasound and photoacoustic images of one vertical slice through the tumor. (b) Before irradiation and (c) after irradiation (808 nm for 2 min, in region left of the marker curve), essentially all cells were killed. (d)–(f) Converting light absorption into heat by the photothermal effect of AuRNBs and PBS. (g)–(i) The NIR laser for pretreatment, treatment after 2 days and 14 days.

Three-dimensional ultrasound and photoacoustic images of the tumor site and its surroundings were acquired before and up to 16 h after injection (Fig. 3a). We found that mice injected with AuRNBs showed a significant increase of photoacoustic signal at the tumor site compared with injection with pure AuR. The images from different time intervals were aligned with one another using simple vertical translations to account for small vertical movements in the transducer positioning. This alignment allowed quantification of the photoacoustic signal at all time points using a single region of interest. We then calculated a subtraction photoacoustic image signal between the photoacoustic image taken at 16 h post-injection and the image taken before injection. The photoacoustic signal was calculated by drawing a 3D region of interest around the tumor (tumor boundaries were clearly visualized in the ultrasound images). The quantified photoacoustic signal is increased as a function of time as shown in Fig. S6 (ESI†). At pre-injection, there is no photoacoustic signal at the tumor site. Conversely, at the 16 h post-injection, mice injected with AuRNBs showed a significantly higher photoacoustic signal than mice injected with pure AuR, indicating that the AuRNBs bind to the tumor site more than pure AuR. On average, at 16 h post-injection, the AuRNBs demonstrated 4.7 times higher intensity in photoacoustic signal compared with pure AuR, which is indicative of a promising contrast agent for photoacoustic imaging modalities.

To evaluate photothermal efficacy, MDA-MB-231 cells incubated with AuRNBs for 24 h were irradiated by a NIR wavelength of 808 nm (2 W cm^{-2}) for 2 min. Before and after irradiation, the cells were stained with clacein AM and ethidium homodimer (EthD-1) to characterize cell viability: live cells appeared green and dead cells appeared red. Before irradiation, live cells are highly visible in the entire region as shown in Fig. 3b. After irradiation, the irradiated region (boundary marked by a white dashed line in Fig. 3c) has almost no live cells and the dead cells are stained red, indicating that irradiation has killed almost all the cells. For *in vivo* measurement of light-to-heat efficiency of AuRNBs, infrared thermal mapping apparatus was used to monitor the temperature rise when the 808 nm NIR laser was irradiated onto MDA-MB-231 tumor-bearing nude mouse ($\sim 5.5 \times 5.5$ mm) as shown in Fig. 3d. The mouse was intravenously injected with AuRNB-containing solution (200 μL, 1 mg mL^{-1}) and then anesthetized with isoflurane and the tumor region irradiated with NIR light (2 W cm^{-2}) at 12 h post-injection. During this irradiation for 2 min, the temperature of the tumor site obviously increased from 31.2 to 68.4 °C in the focal region due to electron–phonon and phonon–phonon process of the NIR absorbing AuRNBs (Fig. 3e). Then, another MDA-MB-231 tumor-bearing nude mouse was intravenously injected with 200 μL phosphate saline-buffered solution (PBS buffer). The nude mouse was also irradiated and monitored on the tumor site under the same irradiation conditions. No obvious temperature variation was observed in the control group (Fig. 3f). Fig. 3g–i show the MDA-MB-231 tumor-bearing nude mouse intravenously injected with AuRNBs solution and irradiated for 2 min with NIR laser as pretreatment, and monitored at day 2 and 14. At day 2, the mice had small scars on the skin at the tumor site with a dark gray color, but the scars on the mice fell off at day 14.

In summary, highly biocompatible mesoporous silica nanobeads with pores filled with gold nanorods (AuRNBs), showing a nano-seaurchin structure, were successfully developed for cancer treatment and photoacoustic imaging *in vitro* and *in vivo*. The AuRNBs showed high thermal stability after laser pulses. *In vivo* and *in vitro* photoacoustic imaging studies showed a relative enhancement contrast modality and photothermal therapeutic with exceptionally high heating efficiency. Together with a well-regulated design, the AuRNBs are expected to act as a potential photoacoustic imaging contrast modality with improved biocompatibility and also show effective photothermal therapy for nano-imaging applications.

Notes and references

1 (*a*) S. Y. Emelianov, P. C. Li and M. O'Donnell, *Phys. Today*, 2009, **62**, 34; (*b*) X. Wang, Y. Pang, G. Ku, X. Xie, G. Stoica and L. V. Wang, *Nat. Biotechnol.*, 2003, **21**, 803; (*c*) H. F. Zhang, K. Maslov, G. Stoica and L. H. V. Wang, *Nat. Biotechnol.*, 2006, **24**, 848.
2 (*a*) I. G. Calasso, W. Craig and G. J. Diebold, *Phys. Rev. Lett.*, 2001, **86**, 3550; (*b*) B. T. Cox and P. C. Beard, *J. Acoust. Soc. Am.*, 2005, **117**, 3616.
3 (*a*) K. H. Song, C. Kim, C. M. Cobley, Y. Xia and L. V. Wang, *Nano Lett.*, 2009, **9**, 183; (*b*) G. D. Moon, S. W. Choi, X. Cai, W. Li, E. C. Cho, U. Jeong, L. V. Wang and Y. Xia, *J. Am. Chem. Soc.*, 2011, **133**, 4762; (*c*) Y. Jin, C. Jia, S. W. Huang, M. O'Donnell and X. Gao, *Nat. Commun.*, 2010, **1**, 1.
4 S. Link, C. Burda, B. Nikoobakht and M. A. EI-Sayed, *J. Phys. Chem. B*, 2000, **104**, 6152.
5 (*a*) Z. B. Ge, Y. J. Kang, T. A. Taton, P. V. Braun and D. G. Cahill, *Nano Lett.*, 2005, **5**, 531; (*b*) Y. S. Chen, W. Frey, S. Kim, K. Homan, P. Kruizinga, K. Sokolov and S. Emelianov, *Opt. Express*, 2010, **18**, 8867; (*c*) M. Wang, J. Ma, C. Chen, F. Lu, Z. Du, J. Cai and J. Xu, *Chem. Commun.*, 2012, **48**, 10404.
6 (*a*) P. J. Chen, S. H. Hu, W. T. Hung, S. Y. Chen and D. M. Liu, *J. Mater. Chem.*, 2012, **22**, 9568; (*b*) P. J. Chen, S. H. Hu, C. S. Hsiao, Y. Y. Chen, D. M. Liu and S. Y. Chen, *J. Mater. Chem.*, 2011, **21**, 2535; (*c*) M. Mahmoudi and M. A. Shokrgozar, *Chem. Commun.*, 2012, **48**, 3957.
7 C. M. Cobley, J. Chen, E. C. Cho, L. V. Wang and Y. Xia, *Chem. Soc. Rev.*, 2011, **40**, 44.
8 L. C. Kennedy, L. R. Bickford, N. A. Lewinski, A. J. Coughlin, Y. Hu, E. S. Day, J. L. West and R. A. Drezek, *Small*, 2011, **7**, 169.
9 H. Maeda, *Adv. Enzyme Regul.*, 2001, **41**, 189.
10 X. Huang, S. Neretina and M. A. EI-Sayed, *Adv. Mater.*, 2009, **21**, 4880.

